

An improved two-dimensional agglomerate cathode model to study the influence of catalyst layer structural parameters

Wei Sun^{a,b}, Brant A. Peppley^{b,c}, Kunal Karan^{a,b,*}

^a Department of Chemical Engineering, Queen's University, Dupuis Hall, Division Street, Kingston, Ont., Canada K7L 3N6

^b Fuel Cell Research Centre, Queen's University, Kingston, Ont., Canada K7L 3N6

^c Department of Chemistry and Chemical Engineering, The Royal Military College of Canada, Kingston, Ont., Canada

Received 5 October 2004; received in revised form 7 December 2004; accepted 8 December 2004

Available online 18 January 2005

Abstract

A two-dimensional model for PEM fuel cell cathode has been developed. The model treats the catalyst layer as agglomerates of polymer electrolyte coated catalyst particles. In this improved model, transport of the two charged species – electrons and ions – as well as that of the chemical species within the catalyst layer is considered. In addition, the transport of electrons through the gas diffusion layer is also considered. The model prediction shows that the cathode overpotential inside the catalyst layer is non-uniform influenced by the channel-land geometry, which implies that the implicit constant overpotential assumption in the commonly employed ultra-thin catalyst layer model is not an accurate representation of actual situation and may lead to overprediction of current densities. Unlike a majority of the multidimensional models that predict the current density to be higher either under the flow-channel area or under the land region, our model illustrates that the location of higher current (electrode reaction rate) changes from the region under the flow channel to that under the land area depending on the overpotential. Our simulation results suggest that charge transport, both electron conduction and the proton migration, is as important as oxygen diffusion in determining the overall electrode reaction rate. Using reaction effectiveness factor analysis, we found that catalyst utilization within the agglomerate is extremely poor at high current densities. The two-dimensional model was employed to investigate the effects of catalyst layer structural parameters including Nafion and platinum loadings and distributions on the cathode performance. The model predicts that there is an optimum level of Nafion loading.

© 2004 Elsevier Ltd. All rights reserved.

Keywords: PEM fuel cell; Catalyst layer; Multidimensional models; Catalyst utilization; Nafion loading

1. Introduction

1.1. Modeling of PEMFC

Fuel cells are considered to be a clean, efficient and less noisy source for electricity generation. The polymer electrolyte membrane fuel cell (PEMFC) fuelled by hydrogen has been actively researched due to its advantages such as low-temperature operation, rapid start-up and high power density. The demands to understand fundamental phenomena occurring in fuel cells and to optimize the design of fuel

cell system have driven the research on modelling fuel-cells and their components [1].

The earliest work on PEM fuel cell modelling were those reported by Bernardi and Verbrugge [2,3] and Springer et al. [4]. These models were one-dimensional (1D), isothermal, and steady state but provided insight into fundamentals of the relevant transport phenomena such as water transport through the membrane and gas diffusion in the electrode. More recent 1D models have included a variety of improvements such as simplification of highly nonlinear equations [5], consideration of both non-saturated and supersaturated conditions for water transport within the electrode [6], and accounting for non-isothermal conditions [7].

* Corresponding author. Tel.: +1 613 533 3095; fax: +1 613 533 6637.
E-mail address: karan@chee.queensu.ca (K. Karan).

Several two-dimensional models (2D) for PEMFC have also been proposed. These models can be classified according to the two directions considered. One class of the models considers variation along-the-channel (ATC) and through-the-membrane (TTM), hereafter referred to as 2D ATC model; the other class of the models considers variation in cross-the-channel (CTC) and through-the-membrane (TTM) directions and will be referred to as 2D CTC model. One of the early 2D models was a 2D ATC model presented by Fuller and Newman [8]. In this model, concentrated solution theory was applied to describe the transport of species in the membrane. Nguyen and White [9] proposed a 2D ATC model where the water transport within the fuel cell was described using the model of Springer et al. [4]. Their model was further refined by introducing cooling effect of co-flow and counter-flow exchanger [10]. More recently, Dannenberg et al. [11] presented a 2D ATC model where the cathode catalyst layer was described in terms of agglomerates of catalysts. All the models discussed above are quasi 2D ATC model in that the equations in two dimensions were solved separately. The first true 2D ATC model was reported by Gurau et al. [12]. In their model, a PEM fuel cell was divided into three computational domains where the standard equations for momentum balance, energy transport, continuity and species concentration were employed. Each domain describes humid hydrogen, humid air and liquid water, respectively. Wang et al. [13] presented a comprehensive 2D ATC model where two-phase flow and transport of reactants and products in the cathode were investigated. One of the drawbacks of the ATC model is that it usually considers the overpotential to be constant within the catalyst layer, which as will be shown in the present study is not necessarily a valid assumption. Another limitation of the 2D ATC model is that it cannot be employed to investigate the transport phenomena in the cross-channel direction. Consequently, it cannot be used to investigate the influence of the flow-field geometry on fuel cell electrochemical performance. To analyze the influence of the bipolar plate rib or land, a 2D CTC model was developed by West and Fuller [14]. However, their model neglected electron transport (or infinite conduction was assumed for electron transport), which as will be shown in the present study can significantly influence the location and rate at which electrochemical reaction occurs. Other 2D models include that by Kazim et al. [15] who developed a 2D CTC mathematical model to investigate the inter-digitated flow-field design and by Kulikovskiy [16] who reported simulation of a direct methanol fuel cell. Based on the 2D model, Kulikovskiy [17] presented a quasi three-dimensional (3D) model, which was mainly concerned with the mechanism of mass transport in the cathode compartment of a fuel cell.

One of the first true 3D models was proposed by Dutta et al. [18]. In their model, the control volume approach was applied to solve the governing equations using a CFD solver, FluentTM (Fluent Inc.). In their model, the velocity and pressure distributions in the flow channels and the GDLs were computed by solving 3D Navier–Stokes equations. Electro-

chemical reactions in the catalyst layer were modelled as source and sink terms in the mass balance equations. More recently, Berning et al. [19–21] presented a 3D model where a commercial software package, CFX-4.3 (AEA Technology) was utilized to solve the differential equations. The constitutive equations used in their model were similar to those of Dutta et al.

The models discussed above have employed a variety of approaches to describe the catalyst layer. These approaches are discussed in the following section.

1.2. Modeling of the catalyst layer

Three different approaches have been undertaken in the literature to model the catalyst layer of a PEM fuel cell. In the most simplified approach, the catalyst layer is treated as a boundary or interface between the gas diffusion layer and membrane; such models are referred to as the ultra-thin layer model. For example, in the 3D model of Berning et al. [19], the catalyst layer was simulated as an interface between GDL and membrane. Whereas such simplification is necessary due to limited computational resource, it limits the insight into how various flow-field plate design and operating parameters influence the catalyst performance. More importantly, the thin-layer models may overestimate current density.

In the second approach, the catalyst layer is considered to be a thin-layer fully flooded with liquid water; such a model is called the flooded thin-layer model [22,23]. In this model, oxygen must diffuse through liquid water to reach the reaction sites. However, the convection flow of water continuously produced on the catalyst surface may make it impossible for gas to diffuse to the catalyst layer, because the flow of product water and oxygen are in opposite direction. In order to obtain agreement between model predictions and experimental data, such a model usually requires that the catalyst layer should be very thin ($\leq 5 \mu\text{m}$). In one such model [22], to ensure agreement between model predictions and experimental data, the permeability of oxygen in the electrolyte had to be made three orders of magnitude higher than that obtained experimentally [26].

The third approach treats the catalyst layer in most detail. In this approach, the catalyst layer is considered to be composed of agglomerates of catalyst particles with porous inter-agglomerate space. The inter-agglomerate space may be occupied by the electrolyte and/or a mixture of reactant/product. Such a model is called the agglomerate model, which can be further subcategorized into slab-agglomerate, cylindrical-agglomerate and spherical-agglomerate models. Iczkowski and Cutlip [24] in 1980 were one of the first to report an agglomerate model for fuel cell catalyst layer simulation. Their model was developed to simulate the performance of a phosphoric acid fuel cell. Ridge et al. [25] adopted Iczkowski and Cutlip model for simulation of PEM fuel cell performance. These two models are typical cylindrical-agglomerate models. Recently, Gloaguen et al. [26,27] developed a slab-agglomerate model where they hypothesized that hydropho-

bic gas pores must exist in the catalyst layer. Their simulation showed that agglomerate model was more suitable compared to the flooded thin-layer models for describing the catalyst layer of a PEM fuel cell. More recently, there has been increased interest in spherical-agglomerate models [28–31]. Broka and Ekdunge [28] reported scanning electron micrograph of the catalyst layer and suggested that spherical-agglomerate model was one of appropriate choices for the catalyst layer. Jaouen and coworkers [29,30] applied a spherical-agglomerate model to investigate the mass transport limitation in the PEM fuel cell. They compared scenarios wherein the electrode reaction rate was controlled by three different mechanisms—Tafel kinetics, oxygen diffusion, and proton migration. Their model, however, neglected electron transport in the electrode, which may significantly affect current density distribution. Essentially, all of the agglomerate models discussed above are 1D models. Most recently, Siegel et al. [31] proposed a 2D ATC model in which they adopted the agglomerate model, proposed by Broka and Ekdunge [28], to describe transport phenomena in the catalyst layer.

The objective of the present study was to develop an improved 2D CTC spherical-agglomerate model for PEM fuel cell cathode, which considers transport of all three types of reacting species (electrons, ions and chemical species) participating in the electrochemical reaction within the catalyst layer. The purpose of the present study was to apply the 2D model to improve our understanding of how the catalyst layer parameters influence the local electrode reaction rates. A key aspect of the study was to investigate the nature and extent of reaction rate distribution under the channel and the land area. The agglomerate model was employed to calculate catalyst utilization via an effectiveness factor approach. An important contribution of the study was to demonstrate the strong influence of electron transport through the electrode on the local reaction rates. Our cathode model accounts for both the proton and the electron conductivity. Further, unlike other agglomerate models [11,28–31] wherein the proton conductivity is considered to be constant, the proton conductivity in our model was modeled as a variable to capture the sensitivity of proton conductivity on local relative humidity [32].

2. Model description

Fig. 1 is a schematic representation of a PEM fuel cell cathode. The key components of the half-cell are the flow-field or bipolar plate, the gas diffusion layer or GDL, and the catalyst layer. The membrane is shown but not included in the present model. The dash line region describes the region of interest.

2.1. Physico-electro-chemical processes considered in the model

A number of interlinked physical, electrical, chemical and electrochemical processes occur within the cathode half-cell.

The overall cathode process can be described in terms of the following eight key processes:

- Process 1 (P1) is multi-component diffusion of chemical species in the GDL.
- Process 2 (P2) represents multi-component diffusion of chemical species in the catalyst layer.
- Process 3 (P3) represents oxygen dissolution at the gas–electrolyte film interface.
- Process 4 (P4) describes the diffusion of dissolved oxygen in the electrolyte film surrounding agglomerate.
- Process 5 (P5) describes diffusion of dissolved oxygen inside the agglomerate.
- Process 6 (P6) represents electron conduction in the cathode, both in the GDL and catalyst layer.
- Process 7 (P7) describes proton transport in catalyst layer.
- Process 8 (P8) is a representation of the oxygen reduction reaction on the catalyst surface.

2.2. Description of the catalyst agglomerate

In this study, the catalyst layer is described in terms of a spherical-agglomerate model. This model considers the catalyst layer to be composed of numerous catalyst agglomerates. Each agglomerate is covered by a thin layer of electrolyte. An agglomerate can be thought of as a cluster of individual carbon black particle with platinum catalysts dispersed on its surface. The carbon black particles are held together as a cluster by the electrolyte coating. The agglomerates form a percolating network-like structure wherein the carbon and polymer electrolyte allow selective transport of electrons and protons, respectively.

2.3. Model assumptions

The key assumptions employed in the model are as follows:

- isothermal and steady state operation;
- partial pressure losses in the electrode are only caused by multi-component diffusion;
- agglomerates are spherical in shape, monodispersed, and evenly distributed in the entire catalyst layer;
- local overpotential within an agglomerate is assumed to be constant.

The last assumption was verified by simulation of a single agglomerate structure.

3. Model equations

This section provides a set of mathematical equations that describe the physical, electrical, chemical and electrochemical processes occurring in the PEMFC cathode. The meaning of symbols can be found in the nomenclature. For simulation purposes, a symmetrical half-cell geometry was adopted.

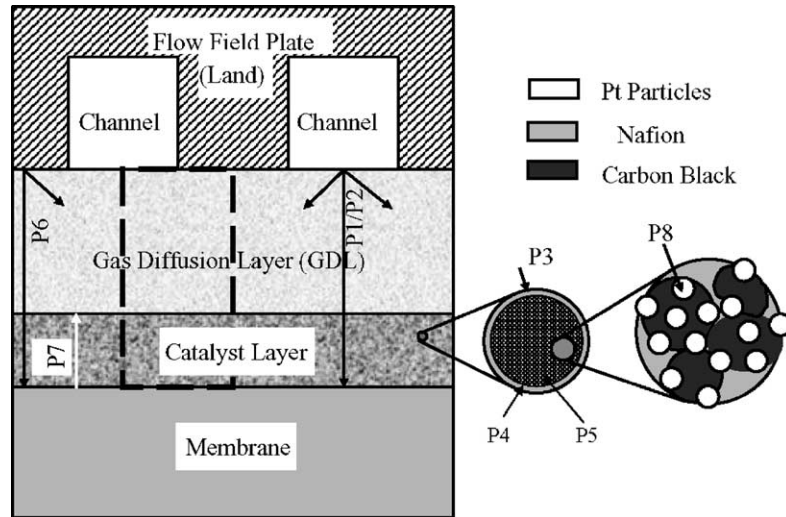


Fig. 1. Schematic diagram of a PEM fuel cell cathode showing key processes.

That is, only half of the channel and half of the land of the flow field were considered, accordingly $x=0$ corresponds to the middle of flow channel, while $x=x_{ld}$ is the middle of channel wall (land).

The computational sub-domains (SDs) and associated dimensions are shown in the Fig. 2 below.

3.1. Species transport in GDL and catalyst layer

Chemical species transport in the GDL and the catalyst layer is described by multi-component diffusion in porous media, which can be described by the following Maxwell–Stefan equations [33]:

$$\nabla \cdot n_i = \nabla \cdot \left[-\rho w_i \sum_j D_{ij}^{\text{eff}} \frac{M}{M_j} \left(\nabla w_j + w_j \frac{\nabla M}{M} \right) \right] \quad (1)$$

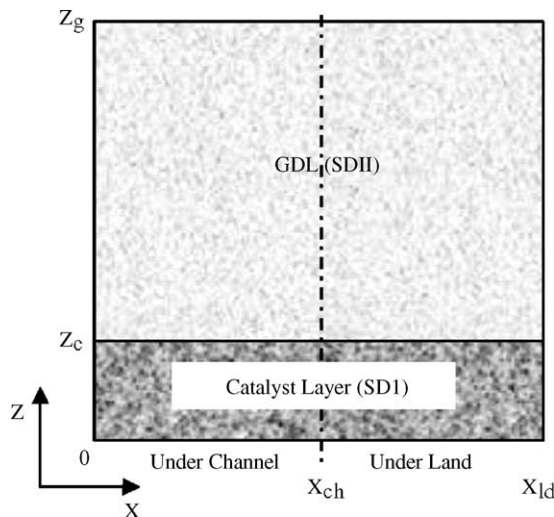


Fig. 2. Sub-domains of simulation.

$$M = \sum_{i=1}^n x_i M_i \quad (2)$$

$$\rho = M \frac{P_{\text{tot}}}{RT_0} \quad (3)$$

Net water drag flux per unit proton flux, α , is accounted for in the water source term, which turns out to be $M_{\text{H}_2\text{O}}(1 + 2\alpha)i/(2F)$. To account for gas diffusion in the porous GDL and catalyst layer, binary diffusion coefficients have been modified to effective diffusivities through the commonly employed Bruggemann relation [2,4,19,28]:

$$\text{In GDL : } D_{ij}^{\text{eff}} = D_{ij} \varepsilon_{\text{GDL}}^{1.5} \quad (4)$$

$$\text{In catalyst layer : } D_{ij,C}^{\text{eff}} = D_{ij} \varepsilon_{\text{CAT}}^{1.5} \quad (5)$$

It is useful to mention that other diffusivity models for GDL have been employed including porosity–tortuosity type correlation [6,18] and, recently reported percolation type correlation [34].

$$D_{ij}^{\text{eff}} = D_{ij} \varepsilon_{\text{GDL}} \left(\frac{\varepsilon_{\text{GDL}} - \varepsilon_P}{1 - \varepsilon_P} \right)^{0.785} \quad (6)$$

The percolation behaviour in the gas diffusion layer may be a better representation of the fibrous porous media; however, in this paper the Bruggemann relation was employed. The impact and validity of different diffusivity models for describing gas diffusion in the fibrous gas diffusion layer is examined elsewhere [35].

3.2. Dissolved oxygen concentration in the polymer electrolyte

In the catalyst layer, oxygen is transported to the catalyst sites as a molecular species dissolved in the polymer electrolyte. The dissolved oxygen concentration at the

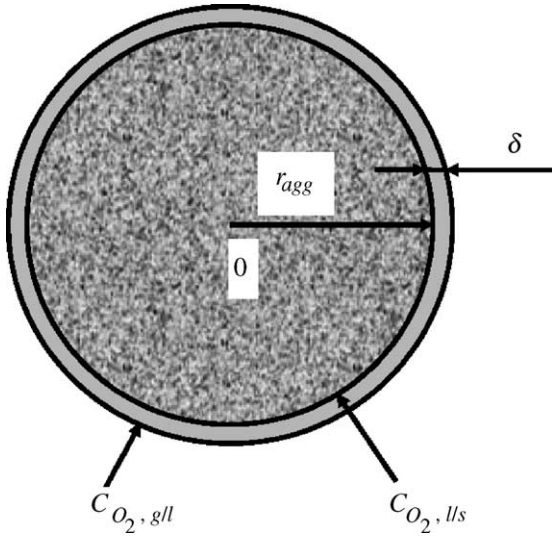


Fig. 3. Agglomerate and its outer electrolyte film size.

gas–electrolyte interface is described by a Henry's law type equilibrium relationship:

$$C_{O_2,gl} = \frac{P_{O_2}}{H} \quad (7)$$

3.3. Diffusion of dissolved oxygen in the electrolyte film covering the agglomerate

For oxygen reduction reaction to proceed, the dissolved oxygen must be transported from the gas–electrolyte interface to the catalyst sites (refer to process P4 in Fig. 1). The transport process can be described as:

$$N'_{O_2} = D \frac{\partial C_{O_2}}{\partial r} \quad (8)$$

It is assumed that the electrolyte film envelopes the agglomerate evenly and that the size of agglomerate is much greater than the electrolyte film thickness as shown in Fig. 3.

Therefore, the dissolved oxygen flux can be calculated by the following equation:

$$N'_{O_2} = D \frac{r_{agg}}{(r_{agg} + \delta)} \frac{(C_{O_2,gl} - C_{O_2,ls})}{\delta} \quad (9)$$

General mass balance on oxygen is applied in the catalyst layer,

$$\nabla \cdot N_{O_2} + a_{agg} N'_{O_2} = 0 \quad (10)$$

$$\nabla \cdot N_{O_2} + R_{O_2} = 0 \quad (11)$$

3.4. Oxygen reduction reaction within the agglomerate

The exact mechanism of oxygen reduction reaction (ORR) is not completely understood [36]. However, it is generally accepted that the slow charge-transfer step for the ORR on Pt catalyst results in a 120 mV/decade ($-2 RT/F$) slope at high

current densities and in a slope half the value (60 mV/decade) at low current density [36]. The overall ORR has been observed to follow first-order kinetics with respect to the oxygen concentration [36].

$$R_{re} = k_c C_{O_2} \quad (12)$$

The overall reaction rate for oxygen consumption in the agglomerate can be expressed in terms the oxygen concentration at the outer surface of agglomerate $C_{O_2,ls}$, an electrochemical reaction rate constant (k_c), and an effectiveness factor of the electrode reaction, E_r :

$$R_{re} = E_r k_c C_{O_2,ls} \quad (13)$$

where, the reaction effectiveness factor for spherical agglomerate is given as follows [37]:

$$E_r = \frac{1}{\Phi_L} \left(\frac{1}{\tanh(3\Phi_L)} - \frac{1}{3\Phi_L} \right) \quad (14)$$

where Φ_L is a dimensionless group, commonly known as Thiele's modulus for chemical reactions:

$$\Phi_L = \frac{r_{agg}}{3} \sqrt{\frac{k_c}{D_{eff}}} \quad (15)$$

$$D_{eff} = D \varepsilon_{agg}^{1.5} \quad (16)$$

3.5. Electrochemical reaction on the catalyst surface

The local volumetric current density in cathode can be described by a Butler–Volmer type kinetics [1,2,23].

$$\nabla \cdot i = a_{Pt}^{eff} i_o^{ref} \frac{C_{O_2}}{C_{O_2}^{ref}} \left[\exp \left(-\frac{\alpha_c F}{RT} \eta_{local} \right) - \exp \left(\frac{(1 - \alpha_c) F}{RT} \eta_{local} \right) \right] \quad (17)$$

The local overpotential can be described as follows:

$$\eta_{local} = E_{local} - E_{th} \quad (18)$$

$$E_{local} = \phi_{s,local} - \phi_{l,local} - \phi_{ref} \quad (19)$$

$$E_{th} = \phi_{s,eq} - \phi_{l,eq} - \phi_{ref} \quad (20)$$

ϕ_{ref} is the reference electrode potential and E_{th} is the theoretical electrode potential of oxygen reduction. The selection of reference electrode influences E_{th} . If oxygen electrode itself is chosen as the reference electrode, implying that the solid phase potential $\phi_s = 0$ V at $z = z_g$, then E_{th} is equal to 0 V. Thus, local electrode potential, E_{local} , can be treated numerically as the local overpotential. If the standard hydrogen electrode (SHE) is used as the reference electrode, $\phi_s = 1.229$ V at $z = z_g$, and E_{th} will be equal to 1.229 V. Therefore, the local overpotential equals the local electrode potential minus E_{th} . The former selection is more convenient than latter one for numerical simulation and is employed in this work.

It must be noted from Eq. (17), that instead of defining exchange current density on a geometric area basis, we have chosen to work with exchange current density based on active or effective platinum surface area, $a_{\text{Pt}}^{\text{eff}}$. This approach allows convenient scaling of platinum loading. To calculate the effective platinum surface area, the actual platinum surface area based on the Pt loading and Pt particle size is first calculated. Next, the surface area actually utilized for the oxygen reduction reaction is accounted for by an effective Pt surface ratio, ε_{I} .

$$a_{\text{Pt}}^{\text{eff}} = \varepsilon_{\text{I}} a_{\text{Pt}} \quad (21)$$

where, a_{Pt} is the specific platinum surface area per unit catalyst layer volume (m^2/m^3), which is equal to the platinum loading divided by the catalyst layer thickness multiplied by the specific surface area of the platinum particles, S_{ac} .

$$a_{\text{Pt}} = \left[\frac{m_{\text{Pt}}}{t_{\text{cl}}} \right] S_{\text{ac}} \quad (22)$$

The surface area per unit mass of an individual Pt particle of radius, r_{Pt} , is given as follows:

$$S_{\text{ac}} = \frac{3}{r_{\text{Pt}} \rho_{\text{Pt}}} \quad (23)$$

The oxygen consumption rate is related to current density according to the following equations [2,3].

$$\nabla \cdot i = -4F \nabla \cdot (N_{\text{O}_2}) \quad (24)$$

$$\begin{aligned} \nabla \cdot i &= 4F R_{\text{O}_2} = 4F R_{\text{re}}(1 - \varepsilon_{\text{CAT}}) \\ &= 4F E_{\text{r}} k_{\text{c}}(1 - \varepsilon_{\text{CAT}}) C_{\text{O}_2, \text{I}} \end{aligned} \quad (25)$$

$C_{\text{O}_2, \text{I}}$ in equation may be written in terms of oxygen partial pressure in gas phase. From Eqs. (10) and (11), the relationship between R_{O_2} and N'_{O_2} can be obtained. By substituting appropriate expressions for R_{O_2} and N'_{O_2} from Eqs. (13) and (9), one can write $C_{\text{O}_2, \text{I}}$ in terms of $C_{\text{O}_2, \text{g}}$. From Eq. (7), $C_{\text{O}_2, \text{g}}$ can be written in terms of P_{O_2} . Consequently, detailed current density divergence is obtained as follows:

$$\nabla \cdot i = 4F \frac{P_{\text{O}_2}}{H} \left(\frac{1}{E_{\text{r}} k_{\text{c}}(1 - \varepsilon_{\text{CAT}})} + \frac{(r_{\text{agg}} + \delta)\delta}{a_{\text{agg}} r_{\text{agg}} D} \right)^{-1} \quad (26)$$

where, k_{c} is reaction rate constant

$$\begin{aligned} k_{\text{c}} &= \left(\frac{\varepsilon_{\text{I}} m_{\text{Pt}} S_{\text{ac}}}{4F t_{\text{cl}}(1 - \varepsilon_{\text{CAT}})} \right) \left[\frac{i_{\text{o}}^{\text{ref}}}{C_{\text{O}_2}^{\text{ref}}} \right] \left[\exp \left(-\frac{\alpha_{\text{c}} F}{RT} \eta_{\text{local}} \right) \right. \\ &\quad \left. - \exp \left(\frac{(1 - \alpha_{\text{c}}) F}{RT} \eta_{\text{local}} \right) \right] \end{aligned} \quad (27)$$

3.6. Charge transport

The proton migration inside the reaction layer can be described by Ohm's law.

$$i_{\text{P}} = -k_{\text{I}}^{\text{eff}} \nabla \phi_{\text{I, local}} \quad (28)$$

where,

$$k_{\text{I}}^{\text{eff}} = k_{\text{I}}[(1 - \varepsilon_{\text{CAT}})\varepsilon_{\text{agg}}]^{1.5} \quad (29)$$

The positive charge transport inside the electrode can also be described by Ohm's law.

$$\text{In the GDL : } i_{\text{e, G}} = -k_{\text{s}} \nabla \phi_{\text{s, local}} \quad (30)$$

$$\text{In catalyst layer : } i_{\text{e, C}} = -k_{\text{s}}^{\text{eff}} \nabla \phi_{\text{s, local}} \quad (31)$$

where,

$$k_{\text{s}}^{\text{eff}} = k_{\text{s}}[1 - \varepsilon_{\text{CAT}}](1 - \varepsilon_{\text{agg}})^{1.5} \quad (32)$$

Conservation of the charge balance leads to the following equations:

$$\text{In the catalyst layer : } \nabla \cdot i_{\text{P}} + \nabla \cdot i = 0 \quad (33)$$

$$\nabla \cdot i_{\text{e, C}} = \nabla \cdot i \quad (34)$$

$$\text{In the GDL : } \nabla \cdot i_{\text{e, G}} = 0 \quad (35)$$

3.7. Boundary conditions

The dimensions of the boundaries discussed in this section are all referred to Fig. 2. At $x=0$ and $x=x_{\text{ld}}$, symmetrical boundary conditions were applied. Therefore, the normal flux of any species, Φ , is assumed to be zero.

$$(\Phi) \cdot n = 0 \quad (36)$$

where, Φ may represent chemical species flux, proton flux and electron flux.

- Boundary conditions for chemical species transport (Eq. (1))

$$x_i = x_{i,0} \quad \text{at } z = z_{\text{g}}, 0 \leq x \leq x_{\text{ch}} : \quad (37)$$

$$(n_i) \cdot n = 0 \quad \text{at } z = z_{\text{g}}, x_{\text{ch}} < x \leq x_{\text{ld}} \text{ and } z = 0 : \quad (38)$$

- Boundary conditions for proton charge balance (Eq. (28))

$$(i_{\text{P}}) \cdot n = 0 \quad \text{at } z = z_{\text{c}} : \quad (39)$$

$$\phi_{\text{I}} = \phi_{\text{I},0} \quad \text{at } z = 0 : \quad (40)$$

- Boundary conditions for electron charge balance (Eqs. (30) and (31))

$$\phi_{\text{s}} = 0 \quad \text{at } z = z_{\text{g}}, x_{\text{ch}} < x \leq x_{\text{ld}} : \quad (41)$$

$$(i_{\text{e, C}}) \cdot n = 0 \quad \text{at } z = 0 : \quad (42)$$

3.8. Solution procedure

The model equations combined with boundary conditions listed in the prior sections are solved with the finite element method using FEMLAB[®]. Stationary nonlinear solver was chosen to solve the highly nonlinear problem. The choice of solution form is General as FEMLAB user's guide recommended [38].

4. Model input parameters

Model input parameters may strongly influence the output of the model simulations. In this study, we made huge effort to select parameters from the original literature sources and have correlated original experimental data with appropriate functional forms.

4.1. Operating and geometric parameters

The operating and geometric parameters are shown in Table 1. A relative humidity of 50% in the flow channel is used in the simulation to simplify the consideration of liquid water flow in electrode. Extending the model to account for two phase flow is under development in our research group.

4.2. Physical and kinetic parameters

The physical and kinetic parameter values for the base case conditions of the present model were selected after a thorough review of the information available in the literature. The parameters employed for base case simulation are presented in Table 2. In the following section, we discuss the range of parameters reported in the literature and, wherever appropriate, provide the rationale for selecting the parameters for our base case simulation.

4.2.1. GDL electronic conductivity

A wide range of GDL conductivity values have been reported for model simulations, ranging from as low as 53 S/m to greater than 10^3 S/m. Bernardi and Verbrugge [3] used a GDL conductivity value of 53 S/m. This value originally reported by Ticianelli et al. [39] was experimentally obtained from high-frequency impedance measurement. Fisher et al. [40] reported that gas diffusion electrode conductivity varies between 50 and 160 S/m depending on different preparation methods. The electrical conductivity data reported by suppliers of commercial GDLs such as Ballard® and Etek® are 100–180 and 80 S/m, respectively [41,42]. Although neglected in a majority of models, it must be recognized that GDL electrical conductivity is likely anisotropic and that the in- and through-plane conductivities may differ significantly. A study is underway in our research group to investigate the anisotropy of relevant transport coefficients of a fibrous GDL [43]. Owing to a lack of reliable anisotropic data, in this paper we assume GDL conductivity to be isotropic and consider an effective conductivity of 100 S/m for base case simulation.

Table 1
Operating and geometric parameters for base case

Operating pressure (absolute) (atm)	1.5
Operating temperature (°C)	80
Oxygen/nitrogen ratio	21/79
Air feed relative humidity (%)	50
Half channel length ($0-x_{cl}$) (mm) ^a	0.5
Half land length ($x_{cl}-x_{ld}$) (mm) ^a	0.5

^a Reference to Fig. 2.

4.2.2. Proton conductivity

The proton conductivity of polysulphonic acid membrane is a function of water content and temperature. Proton conductivity of Nafion as a function of water content has been reported by Springer group [4].

$$k_l = 100 [0.005139\lambda - 0.00326] \exp \left[1268 \left(\frac{1}{303} - \frac{1}{T_o} \right) \right] \quad (43)$$

In the present model, it was assumed that no liquid water would be present in catalyst layer. Thus, as in West et al. [14], relative humidity was used to determine the local water content of the electrolyte phase, λ .

$$\lambda = 0.3 + 10.8RH - 16RH^2 + 14.1RH^3 \quad (44)$$

4.2.3. Catalyst layer thickness

The actual catalyst layer thickness will vary depending on the fabrication method employed and the amount of catalyst loading including Pt/C and Nafion. Typical values reported in the literature range from 5 to 50 μm [32]. Broka and Ekdunge [28] estimated the catalyst layer to be 10–20 μm thick using scanning electron micrograph (SEM) of membrane electrode assembly. Siegel et al. [31] used 100 μm in their model, although the SEM images for the catalyst layer appeared to be 50–80 μm thick. In this study, we have assumed the catalyst layer to be 15 μm in thickness as used in Broka and Ekdunge [28].

4.2.4. Agglomerate dimension

The agglomerate dimension will also depend on the fabrication procedure employed. Broka and Ekdunge [28] reported that the agglomerate diameter ranges 1–5 μm according to their scanning electron micrographs of a PEM fuel cell catalyst layer. Siegel et al. [31] also applied SEM analysis to obtain the mean agglomerate diameter to be about 6 μm . Other researchers [27,29] believe that the agglomerate diameter is around 1 μm . In this paper, we consider the average agglomerate radius to be 1.0 μm , which is probably more representative of current state-of-the-art electrodes for which information has not been published due to proprietary issues.

4.2.5. ORR kinetic parameters

The most comprehensive study of the oxygen reduction reaction at the Pt/Nafion interface was performed by Parthasarathy and coworkers [44–46]. They found that the Tafel plot (log current density versus overpotential) has two distinct slopes, a low slope ~ 60 mV/decade with $\alpha_c = 1$ and a high slope ~ 120 mV/decade with $\alpha_c = \sim 0.5$. The higher value applies at high current densities (so called high slope regime), typically when the cell potential is below 0.8 V. It should be noted that the cathodic transfer coefficient (α_c) is unity for the low slope regime. However, for the high slope

Table 2
Electrode parameters and thermophysical properties for base case

Parameters		Value	Units	Sources
GDL thickness		250	μm	
Porosity of GDL, ε_{GDL}		0.4	–	
Pt loading, m_{Pt}		0.4	mg/cm ²	
Pt particle diameter, r_{Pt}		2.5	nm	
Radius of agglomerate, r_{agg}		1	μm	
Effective specific agglomerate surface area, a_{agg}		3.6×10^5	m ² /m ³	
Catalyst layer thickness, t_{cl}		15	μm	[28]
Porosity of catalyst layer, ε_{CAT}		0.1	–	[31]
Conductivity of GDL, k_s		100	S/m	[25]
Cathodic transfer coefficient ^a , α_c	Low slope (≥ 0.8 V)	1	–	[45]
	High slope (< 0.8 V)	0.61	–	
Reference exchange current density ^a , i_o^{ref}	Low slope (≥ 0.8 V)	3.85×10^{-8}	A/cm ²	[45]
	High slope (< 0.8 V)	1.5×10^{-6}	A/cm ²	
O ₂ diffusivity in Nafion ^a , D		8.45×10^{-10}	m ² /s	[45]
Henry's constant ^a , H		0.3125	atm m ³ mol ⁻¹	[46]
Ref. O ₂ concentration ^b , $C_{\text{O}_2}^{\text{ref}}$		0.85	mol/m ³	[45]
Thickness of electrolyte film covering each agglomerate, δ		80	nm	[51]
Electrolyte fraction in agglomerate, ε_{agg}		0.5	–	[16]
Effective Pt surface ratio, ε_1		0.75	–	[55]
Binary diffusivities	PD _{O₂,H₂O}	3.70×10^{-5}	atm m ² /s	[56]
	PD _{O₂,N₂}	2.79×10^{-5}	atm m ² /s	
	PD _{N₂,H₂O}	3.87×10^{-5}	atm m ² /s	

^a 80 °C.

^b 80 °C and 1.5 atm air.

regime, the transfer coefficient varies with temperature according to the following relationship [45]:

$$\alpha_c = 0.495 + 2.3 \times 10^{-3}(T - 300) \quad (45)$$

According to Parthasarathy et al. [45,46], the reaction order with respect to oxygen is unity. Thus, the exchange current density is directly proportional to oxygen partial pressure and can be described according to the following relationships [45,46].

For low slope regime:

$$\log(i_o) = \log(P_{\text{O}_2}) - 7.89 \quad \text{at } T = 323 \text{ K} \quad (46)$$

For high slope regime:

$$\log(i_o) = \log(P_{\text{O}_2}) - 5.64 \quad \text{at } T = 323 \text{ K} \quad (47)$$

The temperature dependency of the exchange current density can be correlated by an Arrhenius-type relationship

$$i_{o,2} = i_{o,1} \exp \left[-\frac{\Delta E_{\text{exc}}}{R} \left(\frac{1}{T_2} - \frac{1}{T_1} \right) \right] \quad (48)$$

The activation energies ΔE_{exc} for low slope regime and high slope regime were estimated to be 76.5 and 27.7 kJ/mol, respectively by fitting Eq. (48) to the experimental data of Parthasarathy et al. [45].

Beattie et al. [47] have reported a similar relation for oxygen reaction at high slope regime.

$$\log(i_o) = \log(P_{\text{O}_2}) - 3.45 \quad (49)$$

$$\log \left(\frac{i_{o,1}}{i_{o,2}} \right) = -3041.4 \left(\frac{1}{T_1} - \frac{1}{T_2} \right) \quad (50)$$

Beattie et al. [47] attributed the high activation energy at high slope regime (~ 58 kJ/mol) to errors associated with their experimental method. Therefore, in the present study, the data reported by Parthasarathy et al. were employed.

4.2.6. Oxygen diffusivity in NafionTM

Oxygen diffusivity in NafionTM membrane has also been investigated by Parthasarathy et al. [45]. We correlated the data reported by Parthasarathy et al. [45] to obtain the oxygen diffusivity variation with temperature according to the following equation:

$$D = 0.0438 \exp \left(-\frac{E_d}{RT} \right) \quad (\text{in cm}^2/\text{s at } T = 323 \text{ K}) \quad (51)$$

The activation energy for diffusion, E_d , has been determined to be 25 kJ/mol by fitting the reported data [45].

4.2.7. Henry's constant and oxygen solubility

Parthasarathy et al. [46] reported that the Henry's law constant for oxygen in air equilibrated NafionTM at 50 °C is 0.265 atm m³ mol⁻¹. Beattie et al. [47] reported the Henry's constant to be 0.348 atm m³ mol⁻¹, which is of the same order of magnitude as that reported by Parthasarathy et al. For consistency sake, in this paper, the Henry's law constant reported by Parthasarathy et al. [46] was adopted. The variation of Henry's law constant with temperature can be described alternatively in terms of variation of oxygen solubility with

temperature. This is true because Henry's law constant and oxygen solubility are correlated at a given operating pressure via Eq. (7). The effect of temperature on the oxygen solubility is as follow [45]:

$$C_{O_2,2} = C_{O_2,1} \exp \left[-\frac{\Delta G_s}{R} \left(\frac{1}{T_2} - \frac{1}{T_1} \right) \right] \quad (52)$$

The free energy of dissolution, ΔG_s , was determined to be 5.21 kJ/mol by fitting reported experimental data [45].

4.2.8. Nafion electrolyte loading

The Nafion electrolyte loading in the catalyst layer depends on the MEA fabrication method. Lee et al. [51] found that a Nafion loading of 0.6–1.9 mg/cm² may improve for PEMFC performance. They further confirmed the existence of a thin electrolyte film outside of catalyst agglomerates. The estimated thickness of the film ranges from 50 to 80 nm depending on the Nafion loading. The Nafion volume fraction in catalyst layer reported in the literature ranges from 0.3 to 0.72 [16,27,29,31,52]. In this work, the Nafion volume fraction was assumed to be 0.5.

4.2.9. Actual and effective platinum catalyst area

The actual specific area of platinum catalyst can be calculated assuming spherical particles. However, only those Pt particles on the triple phase boundary are useful to the electrode reaction. The effective platinum surface area available for the oxygen reduction reaction was assumed to be 75% of platinum loading surface area for a good preparation [53,54]. This value was also consistent with the experimental results obtained by Li and Pickup recently [55], where they suggested that there is 24% of the catalyst isolated either ionically or electronically.

4.2.10. Gas diffusion coefficients

Binary gas diffusion coefficients for oxygen, nitrogen and water were obtained from Bird et al. [56].

4.2.11. Water flux

A few models [13,34,48,49] have considered the net water flux from anode to cathode, which is a combined effect of electro-osmotic drag, liquid water diffusion and in some instances, the pressure difference between cathode and anode compartments. The net drag coefficient of water molecule per proton used in the literature varies from 0.1 to 1. Those models using higher value (close to 1) may not consider water back diffusion, which affects net drag coefficient significantly at higher current density. Choi et al. [50] have experimentally determined that the coefficient is a constant of 0.3 when the current density is greater than 200 mA/cm² and may be as high as 0.55 at 60 mA/cm². Obviously, this coefficient is dependent on the membrane type and thickness. In this paper, the data reported by Choi et al. [50] were correlated to obtain a relationship between the coefficient and current density, and a relationship between the coefficient and nominal cathode

overpotential, NCO (explained later):

$$\alpha = 46NCO^2 - 31.52NCO + 5.7 \quad (0.25 \text{ V} \leq NCO \leq 0.35 \text{ V}) \quad (53)$$

$$\alpha = 0.3 \quad (NCO > 0.35 \text{ V}) \quad (54)$$

$$\alpha = 1 \quad (NCO < 0.25 \text{ V}) \quad (55)$$

5. Results and discussion

Initially, simulations were conducted to investigate the general trends in overpotential distribution, current density distribution, and catalyst effectiveness. Subsequently simulations were done to study the impact of catalyst layer structural parameters such as Nafion loading, catalyst loading, agglomerate size, and Nafion film thickness on the cathode performance.

5.1. General results

5.1.1. Cathode polarization curve

Fuel cell performance is most commonly evaluated in terms of the steady-state current density–voltage or polarization curve. Fig. 4 shows the steady-state polarization curve generated by our model for base case conditions. The cathode potential shown in Fig. 4 is obtained by subtracting NCO from the theoretical oxygen reduction potential. NCO is defined as the potential difference between the solid phase potential at $z = z_g$ ($x_{ch} < x \leq x_{ld}$) and the electrolyte phase potential at $z = 0$ (reference to Fig. 2). The NCO includes the predicted cathode activation overpotential and ohmic losses due to electron resistance in the GDL and catalyst layer as well as the predicted proton resistance in the electrolyte phase of the catalyst layer.

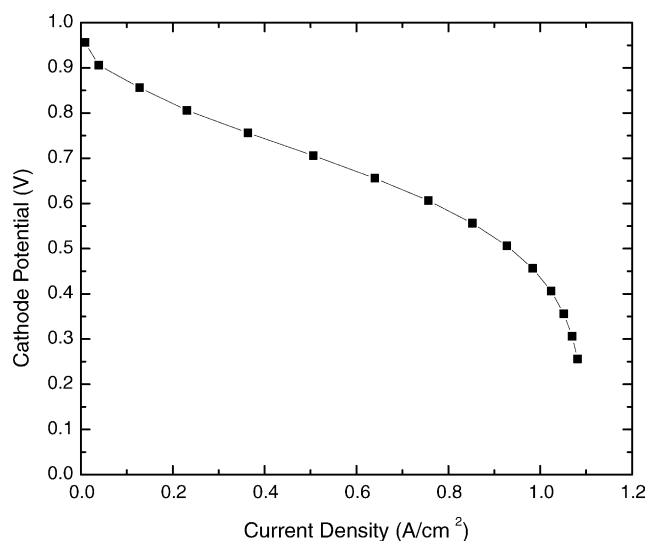


Fig. 4. Cathode polarization curve of base case.

The polarization curve follows the typical trend observed in experimental studies [22,51,57]. It should be pointed out that the ohmic losses in the membrane and the anode overpotential are not included in Eq. (56) and Fig. 4.

$$V = E_{th} - NCO \quad (56)$$

$$E_{th} = 1.229 - 8.456 \times 10^{-4}(T - 298.15) + 4.31 \times 10^{-5}T(\ln[P_{H_2}] + \frac{1}{2} \ln[P_{O_2}]) \quad (57)$$

5.1.2. Local overpotential distribution in catalyst layer

Local overpotential distribution within the catalyst layer for three NCOs: 0.3, 0.5 and 0.7 V, is presented in Fig. 5. The local overpotential is defined as the local potential difference between the solid and electrolyte phases, which reflects the impact of ohmic losses for both electron and proton in cathode on the NCO. Fig. 5 depicts the overpotential variation in the catalyst layer only, i.e. the region between $z=0$ and $z=z_c$ (reference to Fig. 2). Two features are worth noting. Firstly, overpotential within catalyst layer is non-uniform. Secondly, the region where the overpotential is greatest is always under the land area.

It can be observed that at low NCO, the overpotential variation is small but significant. At high NCO (0.7 V), the overpotential variation is as high as 20%. The local reaction rate or current density is related exponentially to the local overpotential and, therefore, small variation in overpotential may lead to a large current density overestimation. As will be shown in the next section, for the case of 0.7 V, the local current density variation exceeds 30%. These findings have implications to the cathode performance predictions from the ultra-thin catalyst layer model, which assumes constant overpotential in catalyst layer and, as such, will overpredict local current densities. This is because the local overpotential at electrolyte/catalyst interface is always lower than NCO due to the consideration of ohmic losses in the GDL and the catalyst layer.

5.1.3. Where does the electrode reaction occur?

One of the objectives of the present study is to investigate the location at which the reaction occurs at the highest rate as well as how the location of maximum reaction rate varies with operating conditions. Fig. 6 presents the oxygen reduction reaction rate distributions for three NCOs, 0.3, 0.5 and 0.7 V that may be considered to represent low, moderate and high overpotentials, respectively. One of the key observations that can be made is that the reaction does not occur uniformly within the catalyst layer.

The simulation results indicate that the location of maximum reaction rate changes with NCO. At low overpotential, more oxygen is consumed under the land area close to membrane. Under low overpotential conditions, the electrode reaction rate is low and oxygen diffuses fast enough to the

reaction sites so that the local activation overpotential is the predominant rate-limiting factor. Electrons travel a shorter distance to the land area than to channel area while protons also migrate shorter distance if the reaction occurs close to membrane. Therefore, the reaction rate is higher at the land area close to membrane. At a moderate overpotential, the maximum reaction rate is predicated to be at the junction between channel and land, where all the reacting species (O_2 , H^+ , e^-) are easily transported. With an increase in overpotential, the maximum reaction rate is predicted to occur in the flow channel area, because oxygen diffusion becomes important. Under higher overpotential conditions, the oxygen consumption is very rapid so that oxygen diffusion becomes the rate-limiting process.

To further illustrate, the distributions of current density at the interface between catalyst layer and membrane ($z=0$), which is total current density, are shown in Fig. 7. It can be seen that the location of maximum current density moves from the region underneath the land to the region under the gas channel as the overpotential increases. We believe that these simulation results are more realistic than those from multidimensional models where the maximum reaction rate (or current density) is predicated to be only in the region under flow channel [19,58]. Kulikovskiy et al. [59] has also found that the most active reaction zone can be either under the channel or under the land area depending on the “choice” of model parameters. However, our model has revealed that different cathode overpotentials cause the location of higher current density to change as well.

5.1.4. Reaction effectiveness factor distribution

The catalyst effectiveness factor is a measure of the extent to which catalyst is utilized and as shown in Eqs. (14) and (15) depends on the effective diffusivity of oxygen and the electrochemical reaction rate constant. An effectiveness factor of unity implies that the reaction occurs uniformly over all of the reaction sites within the agglomerate. As can be inferred from Eqs. (14) and (15), this occurs when reactant diffusion is significantly higher than the reaction. It is important to recognize that an effectiveness factor of unity only implies a uniform utilization of the catalyst and does not imply high reaction rates.

The distribution of the effectiveness factor within the catalyst layer for three NCOs: 0.3, 0.4 and 0.5 V is presented in Fig. 8. Despite the fact that the location of maximum reaction rate or current density shifts from the region under land to under the channel as the overpotential increases, the highest effectiveness factor is observed to always lie in the region under the flow channel area. This is because the local overpotential at this location is less than that in the region under land, and as such the reaction rate constant is low. Consequently, the actual reaction rate is low. Therefore the overall oxygen consumption rate is limited by the slow reaction rate rather by reactant diffusion. At low overpotential (0.3 V), the reaction rate is low, and thus the effectiveness factor distribution is almost uniform and as expected close to unity. With an increase

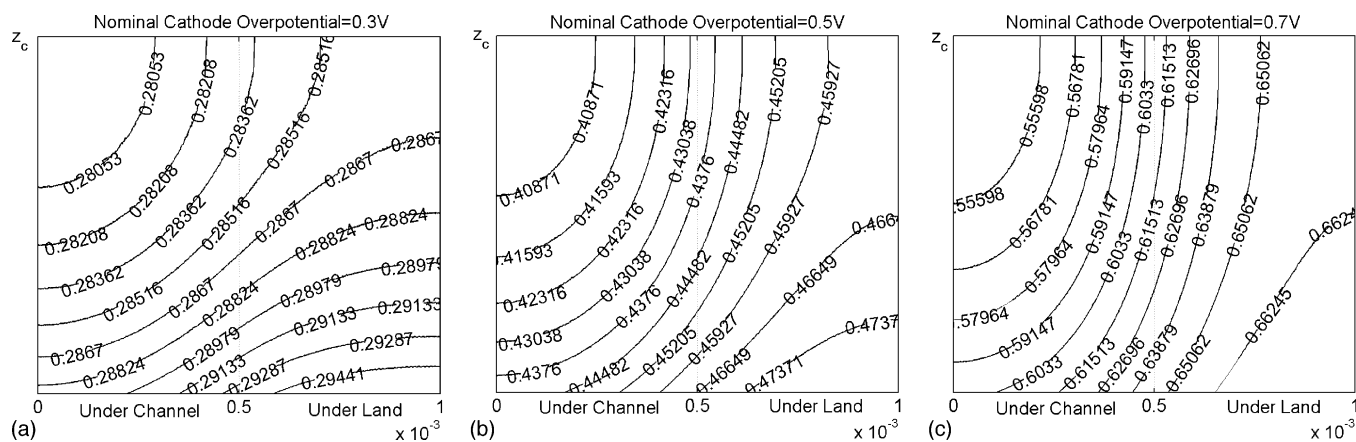


Fig. 5. Local overpotential distribution in the catalyst layer under three different NCOs: (a) 0.3 V, (b) 0.5 V and (c) 0.7 V.

in overpotential, the reaction effectiveness factor distribution becomes significantly non-uniform and may be considered to be extremely low in certain location. For a NCO of 0.5 V, corresponding to an average current density of 640 mA/cm^2 , the maximum effectiveness factor is approximately 0.6 while the minimum is near 0.3. The electrode reaction under the land area occurs mainly on the outer surface of the agglomerates

and the catalytic particles inside the agglomerate contribute less to the reaction.

Prior to discussing the effects of catalyst layer parameters in the next section, it should be noted that the general results predicted above are based on the single-phase consideration, i.e. liquid water accumulation is not included in the present model.

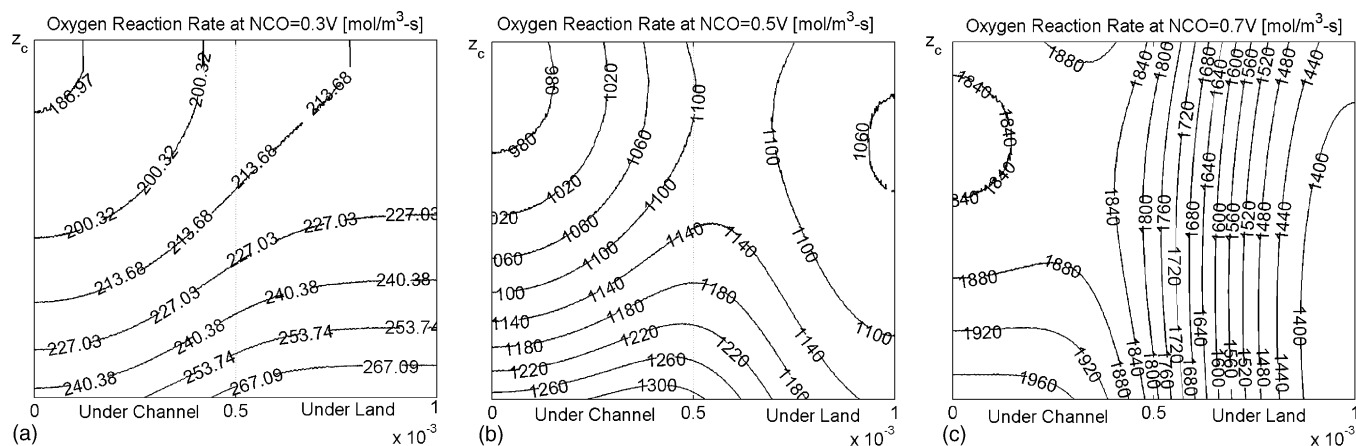


Fig. 6. Oxygen reduction reaction rate distribution in catalyst layer for three NCOs: (a) 0.3 V, (b) 0.5 V and (c) 0.7 V.

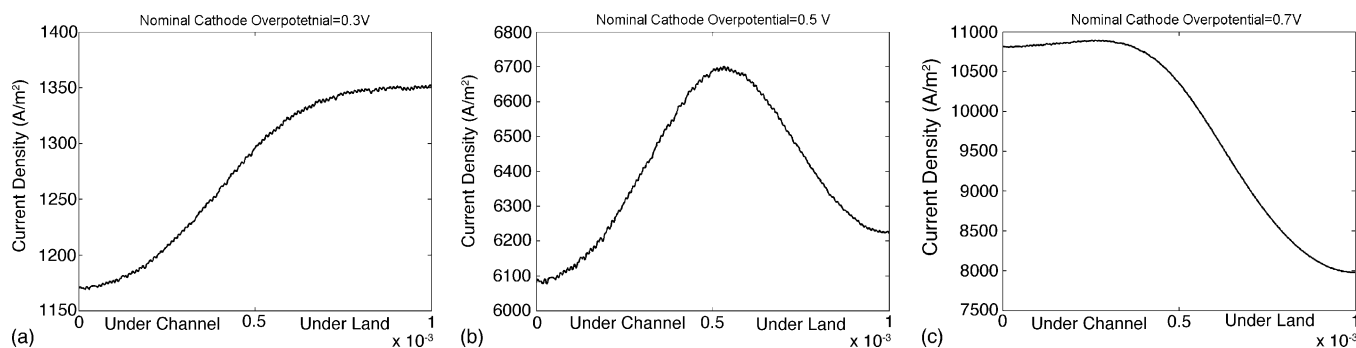


Fig. 7. Current density distribution at the interface between catalyst layer and membrane ($z=0$) for three NCOs: (a) 0.3 V, (b) 0.5 V and (c) 0.7 V.

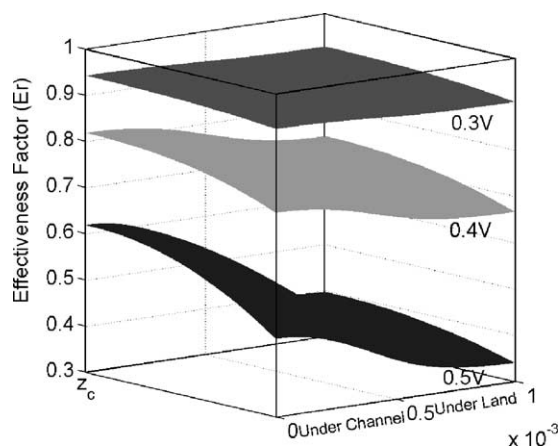


Fig. 8. Effectiveness factor distribution inside catalyst layer for three NCOs: 0.3, 0.4 and 0.5 V (from top to bottom).

5.2. Effects of catalyst layer parameters

5.2.1. Influence of Nafion loading and distribution

It has been reported that to maximize catalyst utilization and improve fuel cell performance, an optimal Nafion loading in the catalyst layer is required [60]. Simulations were conducted to determine whether the model would predict this behaviour and for what conditions the effect would be maximized. For the simulation, the volume fraction of solid phase was kept constant while the Nafion loading was varied. The catalyst layer is composed of solid phase (Pt/C), electrolyte phase (Nafion) and open pores. It must be recognized, therefore that an increase in the Nafion fraction in the catalyst layer results in a decrease in catalyst porosity.

Fig. 9 shows how the current density changes with Nafion loading at a NCO of 0.5 V. Here the volume fraction of solid phase was kept constant at 0.45 of the total catalyst layer volume. From Fig. 9, it can be seen that the cathode performance improves with an increase in the Nafion volume fraction up to

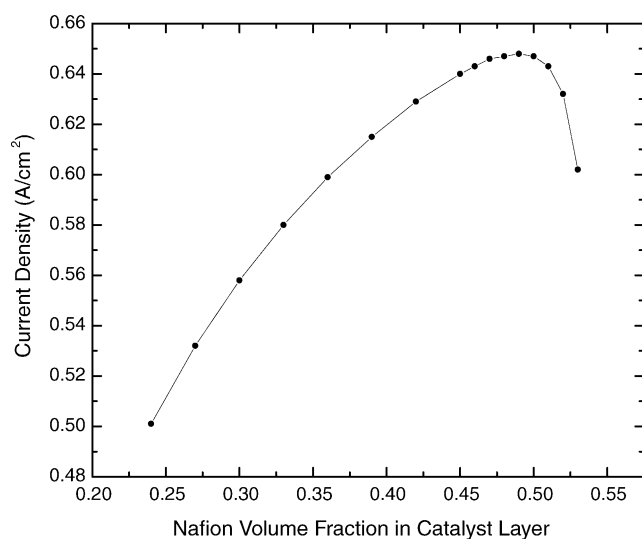


Fig. 9. Effect of Nafion volume fraction on current density. NCO = 0.5 V.

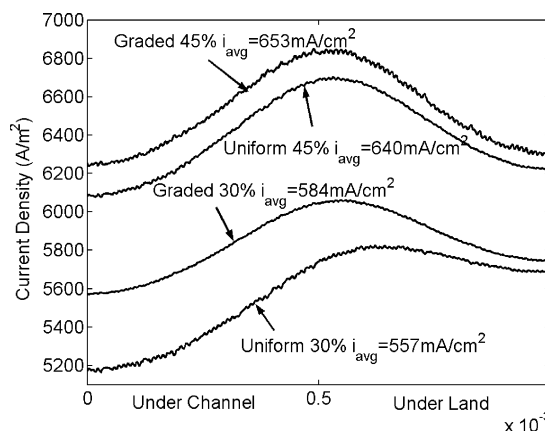


Fig. 10. Current density distribution at $z=0$ for different Nafion loadings and distributions. NCO = 0.5 V.

about 0.48 and then decreases with further increase in Nafion content (e.g. decreasing porosity). Our model clearly captures the experimentally observed phenomenon that an optimum Nafion loading exists with respect to fuel cell performance. For the Nafion fraction between 0.22 and 0.48, the improvement in cathode behaviour is due to the reduction of proton transport limitations in the agglomerate. The current density at Nafion fraction of 0.48 is approximately 30% higher than that at Nafion fraction of 0.25. When the Nafion fraction is greater than 0.5, the current density decreases dramatically. This is attributed to an increase in oxygen transport resistance as the catalyst layer porosity becomes less than 5%. It should be emphasized that this simulation was carried out with the assumption that no liquid water exists in the catalyst layer. If we include a fractional liquid water saturation in the pores of 0.05–0.10 [20], the optimal Nafion volume fraction is estimated to be approximately 40%, which is consistent with experimental results reported in the literature [60,61]. Taking the densities of wetted Nafion as 1.58 g/cm^3 [62] and catalytic carbon as 2.0 g/cm^3 [20], the optimal Nafion weight fraction predicted from our model was found to be 36%.

The model was also used to study whether a catalyst layer with graded (non-uniform) Nafion content would provide improved fuel cell performance. Li and Pickup [55] proposed that more Nafion fraction near the membrane and less near the GDL might improve fuel cell behaviour. In our work, we simulated two cases with linearly varying Nafion content in the catalyst layer. In the first case, the Nafion volume fraction was set to be 54% at the interface between catalyst layer and membrane, and decreased linearly to 6% at the interface between catalyst layer and the GDL. For the second case, the Nafion content on membrane side was kept the same (i.e. 54%), but 36% was used at the GDL side. The average Nafion volume fractions for the two cases were 30% and 45%, respectively. It must be recognized that because the catalyst (Pt/C) volume fraction is kept constant, by considering a varying Nafion fraction we implicitly consider the catalyst layer porosity to vary.

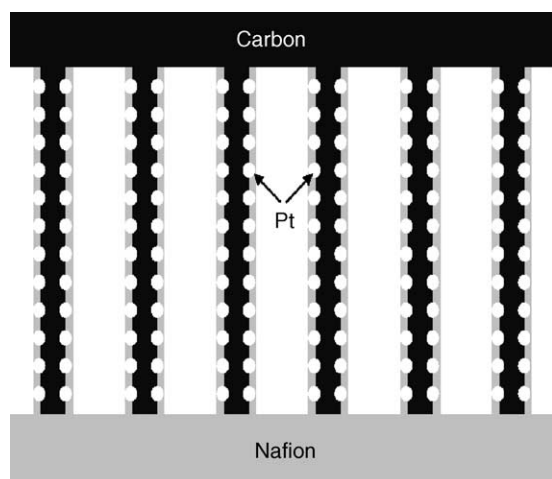


Fig. 11. New electrode structure with all Pt particles equally utilized.

Fig. 10 shows the total current density distribution at $z = 0$ for $\text{NCO} = 0.5 \text{ V}$ for the two graded Nafion loading cases as well as that for uniform Nafion loading corresponding to an average Nafion volume loading of 30% and 45%. The average current densities (i_{avg}) for the four simulation cases are also shown in the figure. From Fig. 10, it can be seen that the graded Nafion distribution cases improves the performance by 5% and 2%, respectively. The improvement may be considered small but significant. The current density difference between the graded cases and the uniform cases is larger in the region under the channel area than that under the land area, which indicates that the improved performance is due mainly to the enhancement in gas transport.

5.2.2. Catalyst loading effects

One of the objectives of the modelling work was to study the influence of catalyst loading on the overall performance of the fuel cell. In this study, in addition to the base case condition of 0.4 mg/cm^2 , we simulated the effect of two lower platinum loadings— 0.1 and 0.05 mg/cm^2 . Usually when a lower platinum loading is employed, the platinum particle size would become smaller. For the base case, a platinum loading of 0.4 mg/cm^2 was used with an average platinum particle diameter of 2.5 nm . Therefore, for the lower Pt loading cases, the Pt diameter was assumed to be 2 nm .

For the case of 0.05 mg/cm^2 the effectiveness factor was set to be equal to 1. This was done to simulate special electrode structures that may allow all the catalyst particles to be utilized equally. Two examples of such electrodes are the catalyst layer prepared by pulsed laser deposition [63] and the new electrode structure being developed by 3M[®] [64]. In both of the examples the catalysts are located on the external surface of agglomerate. A hypothetical electrode structure where all catalysts can be utilized can be represented in Fig. 11.

The cathode polarization curve for the three cases is shown in Fig. 12. From the figure, it can be seen that cathode potential is lowered with a reduction in Pt loading. The reduced

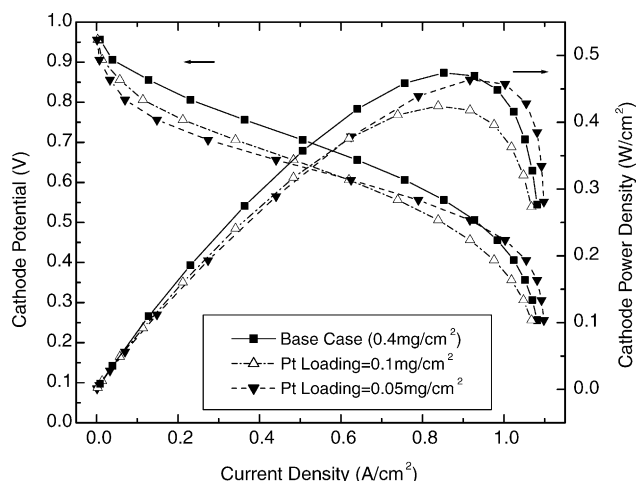


Fig. 12. Comparison of cathode polarization curve for different platinum loading: base case 0.4 , 0.1 and 0.05 mg/cm^2 ($E_r = 1$).

loading results in a decrease in the effective catalyst surface, and expectedly in a reduced electrode reaction rate constant. At lower current densities, the effectiveness factor is usually close to one and the current produced is directly proportional to the Pt loading. However, at higher current densities, owing to slower dissolved oxygen diffusion, the catalysts in the interior of agglomerate access oxygen at concentrations significantly lower than those closer to the outer surface of the agglomerate.

From the Fig. 12, it can be seen that at current density greater than 600 mA/cm^2 , the cathode potential for 0.05 mg/cm^2 case is higher than 0.1 mg/cm^2 . This difference is more noticeable at limiting current density conditions. In addition, the power density peaks for 0.05 and 0.4 mg/cm^2 cases are almost the same.

5.2.3. Agglomerate size effect

It can be readily seen from Eqs. (14) and (15) that a decrease in agglomerate size will lead to an increase in effectiveness factor. This leads to a reduction in resistance to oxygen diffusion within the agglomerate, thereby allowing more catalyst particles to be exposed to higher oxygen concentration resulting in a higher electrode reaction rate. However, controlling the agglomerate size is one of the most challenging aspects of cathode preparation. Further, it is expected that smaller agglomerate size would also result to some extent in a smaller pore size. This may result in difficulty in oxygen diffusion in gas pores. Our work considers macro-pore diffusion as the only transport path for gas diffusion, which is consistent with a pore size in the catalyst layer to be on the order of a micron [31]. Therefore, $1 \mu\text{m}$ was assumed to be the smallest agglomerate diameter in this simulation.

The impact of agglomerate size on the reaction effectiveness factor is shown in Fig. 13. Besides the base case with an agglomerate diameter of $2 \mu\text{m}$, another case where the agglomerate diameter is reduced to $1 \mu\text{m}$ was considered. From the Fig. 13, it can be seen that the smaller size does improve

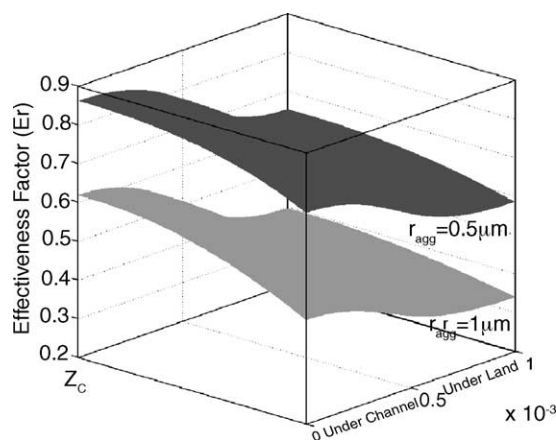


Fig. 13. Effectiveness factor distribution for different agglomerate sizes and distribution. NCO = 0.5 V.

the catalyst utilization. The average effectiveness factor for 1 μm case ($r_{\text{agg}} = 0.5 \mu\text{m}$) rose to over 70% from the base case of 47%.

5.2.4. Agglomerate without electrolyte film

In this study, we have considered an agglomerate to be covered by a uniform layer of electrolyte film. Jaouen et al. [29] have suggested that such a layer of electrolyte film may not necessarily exist as a film covering the agglomerate. In such an agglomerate, the oxygen transport in the cathode will occur in the following steps—diffusion through gas pores, dissolution in the Nafion at the agglomerate surface, followed by reaction and intra-agglomerate diffusion. To demonstrate the impact of considering the presence or absence of electrolyte film covering the agglomerate, simulations were conducted for the case of an agglomerate without an electrolyte film. Although a thin electrolyte film does not cover the agglomerate, some fraction of the agglomerate surface is occupied by electrolyte. Thus, pathways for proton transport exist between agglomerates.

Fig. 14 shows the predicted cathode polarization curves for this case compared to the base case. It can be seen that the electrolyte film surrounding agglomerate is the key factor determining cathode limiting current density. Without the consideration of the film, the cathode potential gradually decreases with the increase in current density. In other words, for the catalyst layer model considering electrolyte-film covered agglomerate, the mass transport limitation is caused by oxygen diffusion in the electrolyte. Recently, the electrode performance from new structure developed by 3M cooperation that utilizes sputter-coated metallic platinum appears to concur with this prediction [64]. This is one of the strengths of such a model, a feature that cannot be captured by thin-film models. However, experimental data on the electrolyte film thickness covering the agglomerate are required to further validate the model.

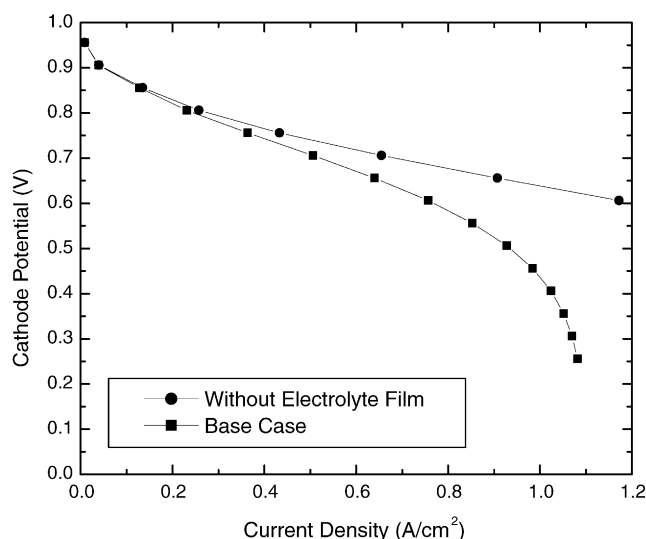


Fig. 14. Comparison of cathode polarization curves for base case and the case of no electrolyte film outside agglomerate.

6. Conclusions

In this study, a 2D agglomerate model was developed to simulate the performance of a PEM fuel cell cathode. In this model, transport of the two charged species—electrons and ions as well as the chemical species within cathode was considered. The model predictions were based on the consideration of single-phase transport and did not account for water accumulation in the GDL and the catalyst layer. It was shown that electron transport in the cathode, neglected in a majority of the previous models, plays an important role in dictating the local electrode reaction rate. The model simulation has yielded a number of key insights concerning electrode performance. It was found that considering the catalyst layer to be infinitely thin leads to an overestimation of current density. Simulation results also show that the reaction rate within the catalyst layer varies significantly with location. An important contribution of this work is to establish that both electron and proton transport in the catalyst layer are important in determining the local cathode overpotential and thereby the electrode reaction rate. The location of maximum reaction rate shifts from under the land to the flow channel depending on the value of total overpotential, indicating that charge transfer in the cathode is as important as oxygen diffusion for determining oxygen reduction rate. Analysis of reaction effectiveness factor distribution indicates that at high overpotentials the catalysts are highly under-utilized.

Model simulations elucidate the impact of catalyst component loadings and distribution on cathode performance. It was found that a catalyst layer with a lower but totally accessible platinum loading may perform better than one with higher loading. Nafion loading also plays an important role in determining cathode performance. Higher Nafion loading increases resistance to oxygen transport while low Nafion load-

ing increases proton migration resistance. Finally, the model indicates that the electrolyte film surrounding the agglomerate is more significant in establishing the limiting current density due to oxygen transport resistance than enhancing electrode performance due to increased proton transport.

Acknowledgements

Authors acknowledge the financial assistance from Natural Sciences and Engineering Council of Canada, DuPont Canada Inc. and Center for Automotive Material and Manufacturing.

Appendix A. Nomenclature

a_{agg}	effective agglomerate surface area (cm^2/cm^3)
a_{Pt}	theoretical platinum loading (m^2/m^3)
$a_{\text{Pt}}^{\text{eff}}$	effective catalyst surface area (m^2/m^3)
B	Tafel slope (V/decade)
C_{O_2}	local oxygen concentration (mol/m^3)
$C_{\text{O}_2, \text{gl}}$	oxygen concentration at the gas electrolyte (mol/m^3)
$C_{\text{O}_2, \text{ls}}$	oxygen concentration at the electrolyte solid (mol/m^3)
$C_{\text{O}_2}^{\text{ref}}$	reference oxygen concentration (mol/m^3)
D	diffusivity of dissolved oxygen in electrolyte phase (m^2/s)
D_{eff}	effective diffusivity of dissolved oxygen in electrolyte inside agglomerate (m^2/s)
$D_{i,j}$	binary diffusivities of species i and j (m^2/s)
D_{ij}^{eff}	effective binary diffusivities of species i and j in GDL (m^2/s)
$D_{ij,C}^{\text{eff}}$	effective binary diffusivities of species i and j in catalyst layer (m^2/s)
E_{local}	local electrode potential (V)
E_r	reaction effectiveness factor
E_{th}	theoretical cathode potential (V)
F	Faraday's constant
H	Henry's constant ($\text{atm m}^3/\text{mol}$)
i_e	electron flux (A/m^2)
i_p	proton flux (A/m^2)
I	current density (A/m^2)
i_o^{ref}	reference exchange current density (A/m^2)
k_c	reaction rate constant (1/s)
k_l	Nafion conductivity (S/m)
k_s	GDL electron conductivity (S/m)
K_l	conductivity of protons in reaction layer (S/m)
K_l^{eff}	effective conductivity of protons in reaction layer (S/m)
K_s^{eff}	catalyst layer electron conductivity (S/m)
M	molecular weight of the gas mixture (kg/mol)
M_i	molecular weight of species i (kg/mol)

m_{Pt}	platinum loading (kg/m^2)
n	normal flux operator
n_i	species mass flux vector ($\text{kg}/(\text{m}^2 \text{ s})$)
N_{O_2}	oxygen mole flux ($\text{mol}/(\text{m}^2 \text{ s})$)
N'_{O_2}	oxygen flux in electrolyte film ($\text{mol}/(\text{m}^2 \text{ s})$)
P_{O_2}	local oxygen pressure (atm)
P_{tot}	total operating pressure (atm)
r_{agg}	radius of agglomerate (m)
r_{Pt}	radius of platinum particle (m)
R	universal gas constant ($\text{J}/(\text{mol K})$)
RH	relative humidity
R_{O_2}	oxygen reaction rate based on catalyst layer volume ($\text{mol}/(\text{m}^3 \text{ s})$)
R_{re}	oxygen reaction rate based on agglomerate volume ($\text{mol}/(\text{m}^3 \text{ s})$)
S_{ac}	actual platinum surface area per mass (m^2/kg)
t_{cl}	catalyst layer thickness (m)
T_o	operating temperature (K)
w_i	mass fraction for component i
x_i	species i molar fraction

Greek letters

δ	thickness of the electrolyte film covering an agglomerate (m)
ε_{agg}	proportion of electrolyte phase in agglomerate
ε_{CAT}	catalyst layer porosity
ε_{GDL}	GDL porosity
ε_l	effective Pt surface ratio
ε_p	percolation threshold
ϕ_l	potential in the electrolyte phase (V)
ϕ_{ref}	reference electrode potential (V)
ϕ_s	potential in the solid electron conductive phase (V)
Φ_L	Thiele's modules
η_{local}	local overpotential (V)
λ	water content
ρ	gas mixture density (kg/m^3)

Subscripts and superscripts

C	catalyst layer
eff	effective
eq	equilibrium state
G	GDL
i, j	gas components in the cathode $i \neq j$
l	electrolyte phase
local	local condition
Pt	platinum
s	solid phase

References

- [1] K.Z. Yao, K. Karan, K.B. McAuley, P. Oosthuizen, B. Peppley, T. Xie, *Fuel Cells Fundam. Syst.* 4 (1–2) (2004) 3.
- [2] D.M. Bernardi, M.W. Verbrugge, *AIChE J.* 37 (8) (1991) 1151.
- [3] D.M. Bernardi, M.W. Verbrugge, *J. Electrochem. Soc.* 139 (9) (1992) 2477.

- [4] T.E. Springer, T.A. Zawodzinski, S. Gottesfeld, *J. Electrochem. Soc.* 138 (8) (1991) 2334.
- [5] G. Murgia, L. Pisani, M. Valentini, B. D'Aguzzo, *J. Electrochem. Soc.* 149 (1) (2002) A31.
- [6] G.J.M. Janssen, *J. Electrochem. Soc.* 148 (12) (2001) A1313.
- [7] A. Rowe, X. Li, *J. Power Sources* 102 (2000) 82.
- [8] T.F. Fuller, J. Newman, *J. Electrochem. Soc.* 140 (1993) 1218.
- [9] T.V. Nguyen, R.E. White, *J. Electrochem. Soc.* 140 (8) (1993) 2178.
- [10] J.S. Yi, T.V. Nguyen, *J. Electrochem. Soc.* 145 (4) (1998) 1149.
- [11] K. Dannenberg, P. Ekdunge, G. Lindbergh, *J. Appl. Electrochem.* 30 (2000) 1377.
- [12] V. Gurau, H. Liu, S. Kakac, *AIChE J.* 44 (11) (1998) 2410.
- [13] Z.H. Wang, C.Y. Wang, K.S. Chen, *J. Power Sources* 94 (2001) 40.
- [14] A.C. West, T.F. Fuller, *J. Appl. Electrochem.* 26 (6) (1996) 557.
- [15] A. Kazim, H.T. Liu, P. Forges, *J. Appl. Electrochem.* 29 (1999) 1409.
- [16] A.A. Kulikovskiy, *J. Appl. Electrochem.* 30 (2000) 1005.
- [17] A.A. Kulikovskiy, *Electrochem. Commun.* 3 (2001) 460.
- [18] S. Dutta, S. Shimpalee, J.W. Van Zee, *J. Appl. Electrochem.* 30 (2) (2000) 135.
- [19] T. Berning, D.M. Lu, N. Djilali, *J. Power Sources* 106 (2002) 284.
- [20] T. Berning, N. Djilali, *J. Electrochem. Soc.* 150 (12) (2003) A1598.
- [21] T. Berning, N. Djilali, *J. Power Sources* 124 (2003) 440.
- [22] T.E. Springer, M.S. Wilson, S. Gottesfeld, *J. Electrochem. Soc.* 140 (12) (1993) 3513.
- [23] C. Marr, X. Li, *J. Power Sources* 77 (1) (1999) 17.
- [24] R.P. Iczkowski, M.B. Cutlip, *J. Electrochem. Soc.* 127 (1980) 1433.
- [25] S.J. Ridge, R.E. White, Y. Tsou, R.N. Beaver, G.A. Eisman, *J. Electrochem. Soc.* 136 (7) (1989) 1902.
- [26] F. Gloaguen, R. Durand, *J. Appl. Electrochem.* 27 (1997) 1029.
- [27] F. Gloaguen, P. Convert, S. Gamburzev, O.A. Velev, S. Srinivasan, *Electrochim. Acta* 43 (24) (1998) 3767.
- [28] K. Broka, P. Ekdunge, *J. Appl. Electrochem.* 27 (1997) 281.
- [29] F. Jaouen, G. Lindbergh, G. Sundholm, *J. Electrochem. Soc.* 149 (4) (2002) A437.
- [30] J. Ihonen, F. Jaouen, G. Lindbergh, A. Lundblad, G. Sundholm, *J. Electrochem. Soc.* 149 (4) (2002) A448.
- [31] N.P. Siegel, M.W. Ellis, D.J. Nelson, M.R. Spakovskiy, *J. Power Sources* 115 (2003) 81.
- [32] T. Thampan, S. Malhotra, H. Tang, R. Datta, *J. Electrochem. Soc.* 147 (9) (2000) 3242.
- [33] C. Curtiss, R. Bird, *Ind. Eng. Chem. Res.* 38 (1999) 2515.
- [34] J.H. Nam, M. Kaviani, *Int. J. Heat Mass Transfer* 46 (2003) 4595.
- [35] K. Karan, W. Sun, J. Pharoah, Proceedings of the Hydrogen and Fuel Cells 2004 Conference and Trade Show On the Effective Diffusivity of Gases in PEM Fuel Cell Electrodes, Toronto, ON, Canada, September 2004.
- [36] J. Lipkowski, P.N. Ross, *Electrocatalysis*, WILEY-VCH, 1998.
- [37] H.S. Fogler, *Elements of Chemical Reaction Engineering*, Prentice Hall Inc., New Jersey, 1999.
- [38] Comsol Inc., 2001. FEMLAB User's Guide and Introduction, Version 2.2.
- [39] E.A. Ticianelli, C.R. Derouin, A. Redonodo, S. Srinivasan, *J. Electrochem. Soc.* 135 (9) (1988) 2209.
- [40] A. Fisher, J. Jindra, H. Wendt, *J. Appl. Electrochem.* 28 (1998) 277.
- [41] http://www.ballard.com/pdfs/AvCarb_P50.pdf (Retrieved date: 18 May 2004).
- [42] http://www.etek-inc.com/pdfs/etek_catalog.com.pdf (Retrieved date: 18 May 2004).
- [43] D. Hamilton, M. Austin, J. Pharoah, Proceedings of the Hydrogen and Fuel Cells 2004 Conference and Trade Show on A Direct Method for Determining Effective Properties in Polymer Electrolyte Fuel Cell Electrodes, Toronto, ON, Canada, September 2004.
- [44] A. Parthasarathy, C.R. Martin, S. Srinivasan, *J. Electrochem. Soc.* 138 (4) (1991) 916.
- [45] A. Parthasarathy, S. Srinivasan, A.J. Appleby, C.R. Martin, *J. Electrochem. Soc.* 139 (9) (1992) 2530.
- [46] A. Parthasarathy, S. Srinivasan, A.J. Appleby, C.R. Martin, *J. Electrochem. Soc.* 139 (10) (1992) 2856.
- [47] P.D. Beattie, V.I. Basura, S. Holdcroft, *J. Electroanal. Chem.* 468 (1999) 180.
- [48] J.S. Yi, T.V. Nguyen, *J. Electrochem. Soc.* 146 (1) (1999) 38.
- [49] P. Berg, K. Promislow, J. Pierre, J. St. Stumper, B. Wetton, *J. Electrochem. Soc.* 151 (3) (2004) A341.
- [50] K.H. Choi, D.H. Peck, C.S. Kim, D.R. Shin, T.H. Lee, *J. Power Sources* 86 (2000) 197.
- [51] S.J. Lee, S. Mukerjee, J. McBreen, Y.T. Rho, T.H. Lee, *Electrochim. Acta* 43 (24) (1998) 3693.
- [52] S. Um, C.Y. Wang, Proceedings of the ASME Fuel Cell Division on Three Dimension Analysis of Transport and Reaction in Proton Exchange Fuel Cells, HTD-Vol. 366-1, Orlando, FL, 2000, p. 19.
- [53] X. Cheng, B. Yi, M. Han, J. Zhang, Y. Qiao, J. Yu, *J. Power Sources* 79 (1999) 75.
- [54] S. Malhotra, T. Thampan, R. Datta, *Electrochem. Soc. Proc.* 99–113 (1999) 256.
- [55] G. Li, P.G. Pickup, *J. Electrochem. Soc.* 150 (11) (2003) C745.
- [56] R.B. Bird, W.E. Stewart, E.N. Lightfoot, *Transport Phenomena*, John Wiley & Sons Inc., New York, 1960.
- [57] J. Kim, S. Lee, S. Srinivasan, C.E. Chamberlin, *J. Electrochem. Soc.* 142 (8) (1995) 2670.
- [58] A. Kumar, R.G. Reddy, *J. Power Sources* 113 (2003) 11.
- [59] A.A. Kulikovskiy, J. Divisek, A.A. Kornyshev, *J. Electrochem. Soc.* 146 (11) (1999) 3981.
- [60] E. Antolini, *J. Appl. Electrochem.* 34 (2004) 563.
- [61] E. Passalacqua, F. Lufrano, G. Squadrito, A. Patti, L. Giorgi, *Electrochim. Acta* 46 (2001) 799.
- [62] L.A. Zook, J. Leddy, *Anal. Chem.* 68 (1996) 3793.
- [63] N. Cunningham, E. Irissou, M. Lefevre, M.C. Denis, D. Guay, J.P. Dodelet, *Electrochem. Solid-State Lett.* 6 (7) (2003) A125.
- [64] 3M Cooperation, Advanced MEA's for enhanced operating conditions, Amenable to high volume manufacture, 2003 DOE Hydrogen, Fuel Cell, and Infrastructure Technology Program Review Meeting, Berkeley, CA, 19–22 May 2003.